

Kazuaki YASUNAGA^{*1}, Kunio YONEYAMA¹, Hisayuki KUBOTA¹, Hajime OKAMOTO², Atsushi SHIMIZU³, Hiroshi KUMAGAI⁴, Masaki KATSUMATA¹, Nobuo SUGIMOTO³, and Ichiro MATSUI³

¹Institute of Observational Research for Global Change, JAMSTEC Yokosuka headquarters, Kanagawa, Japan

²Center for Atmospheric and Oceanic Studies, Graduate School of Science, Tohoku University, Sendai, Japan

³National Institute for Environmental Studies, Tsukuba, Ibaraki, Japan

⁴National Institute of Information and Communications Technology, Tokyo, Japan

1. Introduction

The vertical distribution of radiatively active tracers, aerosols, and clouds influences the earth climate via the radiative properties of the atmosphere. Clouds have the largest radiation-forcing properties. At low latitudes, the short wave flux incident to the top of the atmosphere and long wave radiation flux emitted from the earth surface are large. The vertical distribution of tropical clouds is therefore an important component of understanding the energy balance of Earth.

Over regions of warm tropical sea surface temperatures (SSTs), the atmosphere is conditionally unstable, and many isolated or highly organized convections occur. Johnson et al. (1996) described prominent stable layers at heights of 2 km, 5 km, and 15-16 km, observed during the Tropical Ocean Global Atmosphere Coupled Ocean-Atmosphere Response Experiment (TOGA COARE). Johnson et al. (1999) also found that maxima in the vertical distributions of radar-echo (cloud) tops exist in the vicinity of these three stable layers heights.

It is a well known fact that environmental static stability influences the vertical profiles of detrainment from cumulus convection as well as the top heights of cumulus convection. Yasunaga et al. (2003) performed a statistical analysis of NASA Pacific Exploratory Mission-Tropics B (PEM-Tropics B) observational data and found that tropical cumulus convection directly transported boundary layer air to

**Corresponding author address:* Kazuaki Yasunaga, Institute of Observational Research for Global Change, JAMSTEC Yokosuka headquarters, 2-15, Natsushima-Cho, Yokosuka-city, Kanagawa, 237-0061, Japan; E-mail: yasunaga@jamstec.go.jp

the 350-600 hPa and 750-800 hPa levels. These pressure levels coincide with the heights where stable layers were frequently observed during the PEM-Tropics B. It is therefore reasonable to expect that clouds detrained from cumulus convection ("detrainment shelves" of Mapes and Zuidema, 1996) would be frequently observed at around the specific layers of 2, 5, and 15-16 km as well as cloud tops.

We consider that detrainment shelves are thin cloudy layers composed of small condensate particles of negligible terminal velocity (<0.1 mm in radius). Firstly, in the present study, the frequency distribution of base height of clouds without falling condensate particles (>0.1 mm in radius) is examined, making use of 95 GHz cloud profiling radar (wavelength of 3.16 mm) and lidar with a dual wavelength of 532 nm and 1064 nm. Secondly, thickness of the cloud with little falling condensate particles is estimated with lidar and radiosonde-derived relative humidity.

2. Data and meteorological conditions during MR01-K05 Leg3-4 cruise

The data utilized in the present study were obtained by stationary observation over the tropical western Pacific (around 1.85°N, 138°E) from November 9 to December 9, 2001 by the Research Vessel Mirai of the Japan Marine Science and Technology Center (JAMSTEC). During the intensive observation period (IOP), the principal mission objectives were C-band weather Doppler radar observations, atmospheric sounding by radiosonde, surface meteorological measurement, conductivity-temperature-depth profiler castings to 500 m, and current measurement

by acoustic Doppler current profiler. Additional tasks included turbulent flux measurement, solar radiation measurement, cloud profiling radar (SPIDER), lidar, and greenhouse gas measurement.

The cloud profiling radar (SPIDER) has a frequency of 95 GHz (wavelength of 3.16 mm). The vertical resolution of the radar data was 82.5 m, with the maximum altitude of the observation being 20 km, with a time resolution of about 0.1 seconds. The radar reflectivity factor is commonly indicated in the logarithmic form (dBZe), and the minimum detectable radar reflectivity factor averaged over 1 minute was -43 dBZe at 5 km. A full description of the cloud profiling radar SPIDER is provided by Horie et al. (2000).

The lidar utilized in the present study is a two-wavelength (532 nm and 1064 nm) Mie-scattering lidar with a depolarization measurement capability of 532 nm. The original data had a vertical resolution of 6 m and a temporal resolution of 10 seconds. The maximum altitude of observations was 20 km. Technical specifications of the lidar are provided by Sugimoto et al. (2001), while additional details concerning the shipborne cloud profiling radar and lidar system are provided by Okamoto et al. (2005).

Figure 1 shows the infrared equivalent blackbody temperature measured during the IOP by Geostationary Meteorological Satellite of the Japan Meteorological Agency. Westward-propagating and eastward-propagating convective areas reached the site in the first and latter half of the IOP, respectively. According to Madden-Julian Oscillation (MJO) monitoring by the National Oceanic and Atmospheric Administration/Climate Diagnostics Center (<http://www.cdc.noaa.gov/>), eastward-propagating convective areas in the late IOP are identified as MJO signals. In the present study, we use satellite TBB data to simply define the intraseasonal convectively “active” period from the first entry of the eastward-moving large-scale low TBB (<250 K) area into the observational site; other periods are defined as “inactive” (09 November–28 November: inactive period; 29 November–09 December: active period).

Therefore, it should be noted that westward-propagating convective areas in the first half of the IOP are included in the “inactive” period.

Figure 2 presents time-height cross-sections of zonal and meridional winds derived from radiosonde data. Westerly winds were dominant in the lower troposphere during the entire observational period (Fig. 2a). There were two peaks of strong westerly wind during the middle of November and early December, each time accompanied by cloud activities. The meridional wind component shows the periodic replacement of positive and negative values between the 100 hPa and 300 hPa levels (Fig. 2b), which would indicate that equatorial trapped waves prevailed during this period. The periodic variations of the meridional wind are also seen in the mid-level, and would be affected by the upper-level meridional wind variations.

The frequency distribution of temperature lapse rates exceeding the thresholds of -4 , -4.5 , and -5 K km^{-1} are shown in Fig. 3. The results presented in Fig. 3 were calculated for a depth of 500 m. During the IOP, stable layers were frequently observed at the heights of 2 km and 5.5 km, while weakened stability layers were detected at a height of around 4.5 km (Fig. 3a). The frequency distribution of the height of the stable layer during the IOP is similar to that recorded during TOGA COARE (e.g., Johnson et al. 1996).

The stability at 2 km height was more prominent in the inactive period than in the active period (Figs. 3b and 3c). The stable layer at mid-levels was more pronounced in the active period, although the height of the peak was lower in the active period (5 km) than in the inactive period (6 km). While a layer of weakened stability was observed around 4.5 km height during the both periods, the layer was much shallower in the active period.

Figure 4 shows variation in the coverage of C-band radar echoes with reflectivity factors >15 dBZ at 2 km height over a 200×200 km area. Radar echo is classified as either convective or stratiform type, following the method by Steiner et al. (1995). It should be noted that vertical scale is large in the lowest panel in Fig. 4.

The characteristics of precipitation differ between the active and inactive period. During the inactive period (09 – 28 November), precipitation occurred almost daily, and convective type echoes were dominant except on 9 10 and 23 November. In the (MJO) active period (29 November - 09 December), coverage of radar echoes was much larger than in the inactive period, and stratiform type echoes were dominant, which is consistent with the results of Lin et al. (2004).

3. Data analysis and procedures

Radar and lidar data were interpolated to produce consistent vertical and temporal resolution. The combined data used in the present analysis has a vertical resolution of 82.5 m and the time resolution of 1 minute. The base height of cloudy layers with little or no falling condensate particles was determined via the radar reflectivity factor and lidar backscattering coefficient, according to the following three steps.

1. The provisional base level of the cloudy layer (Z_l) is defined as the level at which the lidar backscattering coefficient first exceeds a certain threshold (L_c) during a vertical scan from the height of 2 km. The lidar has two wavelengths, and the lower level is selected as Z_l . The starting height of the vertical scan, 2 km, was selected in order to avoid aerosols and clouds within the boundary layer.
2. The provisional base level of the cloudy layer (Z_r) is defined as the level at which the radar reflectivity factor first exceeds a certain threshold (R_c) during a vertical scan from a height of 2 km.
3. The ultimate base level of the cloudy layer (Z_b) is defined by Z_l for the case where the height of Z_l is less than that of Z_r , or where Z_l is defined and Z_r cannot be determined. Z_b is considered to be indefinite in the case of the height of Z_r being equal to or lower than that of Z_l , or when Z_l cannot be determined.

Radar is more sensitive than lidar in terms of falling condensate particles (radius >0.1 mm), and is able to detect such large particles at lower levels than lidar,

provided an adequate R_c value is chosen. Therefore, when the height of Z_r is equal to or lower than that of Z_l , we can conclude that falling condensate particles exist. This forms the basis of defining Z_b as indefinite in the third step outlined above. Conversely, lidar is more sensitive to small particles of negligible terminal velocity (<0.1 mm in radius) than radar. Accordingly, when the height of Z_l is lower than that of Z_r , or when Z_r is indefinite, Z_l can be considered to represent the base height of a cloudy layer with little or no falling condensate particles.

Figure 5 shows observations made on 10 November 2001. In this case, L_c and R_c are -5.25 ($= \log_{10} \beta$, where β ($m^{-1} sr^{-1}$) is the backscattering coefficient) and -35 dBZe, respectively. During 0100-0200 UTC, the lidar backscattering coefficient is large around the height of 5 km, while high radar reflectivity is recorded at lower levels. These observations indicate that falling condensate particles exist, and that Z_b is defined as indefinite (see the lower panel in Fig. 5). In contrast, during 0400-0500 UTC and 2000-2200 UTC, lidar detects thin cloudy layers at mid-levels (5-7 km), while the cloud profiling radar detects only weak (or no) signals. Although attenuation effects prevent lidar from observing structure above the optically thick cloud, the high relative humidity areas indicate the reality of the cloud thickness observed with lidar. Images from the total sky imager (TSI), a full-color digital imaging and software system designed to automatically monitor cloud conditions, support the existence of thin cloudy layers (Figs. 6a and 6b). While the TSI cannot identify the height of the cloud, neither lidar nor cloud profiling radar showed strong signals above the height of 8 km. Therefore, the thin cloudy layers in the Figs. 6a and 6b would be located at the mid-levels with large backscattering coefficients of lidar (Fig. 5). This example clearly demonstrates that the thickness of the cloud with little falling condensate particles detected in the present analysis procedure is thin.

4. Results

Figure 7 shows the frequency distribution of the

measured base heights of cloudy layers. L_c varies from -4.25 to -5.25 ($= \log_{10} \beta$, where β ($\text{m}^{-1} \text{sr}^{-1}$) is the backscattering coefficient) at 0.25 intervals, while R_c varies from -10 to -35 dBZe at 5 dBZe intervals. Values averaged over 30 (5 x 6) samples are displayed in Fig. 7. The error bars indicate the ranges within one standard deviation as calculated from the 30 samples.

A peak exists between the heights of 4.5 and 6.5 km during the IOP (Fig. 7a). During the inactive period, when coverage of the convective type echoes were as large as that of the stratiform type echoes (Fig. 4), two peaks are found around the heights of 6 and 7 km (Fig. 7b). The peaks coincide with the height of the frequent occurrence of the stable layer. In the active period, when coverage of the stratiform type echoes was much greater than convective type echoes (Fig. 4), there are two peaks around the heights of 5 and 6 km (Fig. 7c). The levels of the both peaks also agree with the height of the stable layers. Although the characteristics of precipitation are different between in the inactive and active periods, the peak between the heights of 4.5 km and 6.5 km is apparent in the both periods. The mid-level peak apparent in Fig. 7a, therefore, does not reflect a specific event. The frequent occurrence of the base of cloudy layers around 4.5 – 6.5 km height is presumably a general phenomenon over warm tropical oceans. The heights of the peaks in Fig. 7 do not vary when the starting height of the vertical scan is changed from 0 km to 2 km.

Figures 8 and 9 show examples in which the base of cloudy layers was observed between the heights of 4.5–6.5 km. In Fig. 8, the base of the cloudy layers occurs at mid-levels during 0300–0400 UTC, 1000–1400 UTC, and 1900–2100 UTC. The thickness of observed cloudy layers is relatively thin. Figure 9 shows the occurrence of mid-level thin cloudy layers for almost the entire day. TSI images and radiosonde-derived relative humidity support the existence and thin thickness of the cloudy layers detected with the present analysis procedure (Figs. 8d, 9d, 10a and 10b).

When clouds are identified as objects with a lidar

backscattering coefficient exceeding a certain threshold, almost all of the clouds whose base heights (Z_b) are detected between at 4.5 – 6.5 km height had a thickness smaller than 500 m (Table 1). Clouds are also identified with relative humidity derived from radiosonde, which was launched every 3 hour, because attenuation effects prevent lidar from observing structure above the optically thick cloud. In the relative humidity case, 60 – 70 percent of the clouds had the thickness smaller than 500 m (Table 2). Thick cloudy layers, therefore, are unlikely to exist above the cloud bases determined with the analytical method described in the present study (Z_b). As a result, the frequency peak of the base heights of mid-level cloudy layers shown in Fig. 7 can be regarded as representing the frequency occurrence of mid-level thin clouds. This interpretation is also consistent with the vertical cloud distribution inferred from radiosonde-derived relative humidity data (Mapes and Zuidema, 1996).

5. Discussions

The peak of the frequency distribution of thin cloudy layers (Fig. 7) is located near the stable layer often observed (Fig. 3). Accordingly, part of the thin cloud probably represents detrainment shelves from the convective cloud that was enhanced by the stable layer. The upper peak in the inactive period (Fig. 7b) agrees with the detrainment level estimated by Zuidema (1998) (400 hPa). The lower peak in the inactive period (Fig. 7b) and the upper peak in the active period (Fig. 7c) are consistent with the Bretherton and Smolarkiewicz (1989) model (500 hPa). The lower peak in the active period (Fig. 7c) coincides with the detrainment level estimated by Mapes (2001) (600 hPa). The peak levels of the frequency distribution of thin cloudy layers observed in the present study, therefore, seem to support all results obtained in the previous works.

References

Horie, H., T. Iguchi, H. Hanado, H. Kuroiwa, H.

Okamoto, and H. Kumagai, 2000: Development of a 95-GHz Airborne Cloud Profiling Radar (SPIDER): Technical Aspects, *IEICE Trans. Commun.*, E83-B(No.9), 2010- 2020.

Johnson, R.H., P.E. Ciesielski, and K.A. Hart, 1996: Tropical inversions near the 0°C level, *J. Atmos. Sci.*, **53**, 1838-1855.

-, T. M. Rickenbach, S. A. Rutledge, P. E. Ciesielski, and W. H. Schubert, 1999: Trimodal characteristics of tropical convection, *J. Climate*, **12**, 2397-2418.

Lin, J., B. Mapes, M. Zhang, and M. Newman, 2004: Stratiform Precipitation, Vertical Heating Profiles, and the Madden-Julian Oscillation, *J. Atmos. Sci.*, **61**, 296-309.

Mapes, B. E., and P. Zuidema, 1996: Radiative-dynamical consequences of dry tongues in the tropical troposphere, *J. Atmos. Sci.*, **53**, 620-638.

Okamoto, H., T. Nishizawa, T. Takemura, H. Kumagai, H. Kuroiwa, N. Sugimoto, I. Matsui, A. Shimizu, A. Kamei, S. Emori, T. Nakajima, Vertical cloud structure observed from shipborne radar and lidar, 2005: Part (I): mid-latitude case study during the MR01/K02 cruise of the R/V *Mirai*, *submitted to J. Geophys. Res.*

Steiner, M., R. A. Houze Jr. and S. E. Yuter. 1995: Climatological Characterization of Three-Dimensional Storm Structure from Operational Radar and Rain Gauge Data. *J. Appl. Meteor.*, **34**, 1978-2007.

Tokay, A., and D. A. Short, 1996: Evidence from tropical raindrop spectra of the origin of rain from stratiform versus convective clouds, *J. Appl. Meteor.*, **35**, 355-371

Sugimoto, N., I. Matsui, and A. Shimizu, 2000: Climatological characteristics of cloud distribution and planetary boundary layer structure in Jakarta, Indonesia revealed by lidar observation, *Geophys. Res. Lett.*, **27**, 2909-2912.

Sugimoto, N., I. Matsui, Z. Liu, A. Shimizu, and K. Asai, 2001: Latitudinal distribution of aerosols and clouds in the western Pacific observed with a lidar on board the research vessel *Mirai*, *Geophys. Res. Lett.*, **28**, 4187 -4190.

Yasunaga, K., H.Kida, and T.Satomura, 2003: The 600-750 hPa relative humidity minimum observed during PEM-Tropics B, *Geophysical Research Letters*, **30**(24), 2282, doi: 10.1029/2003GL018739.

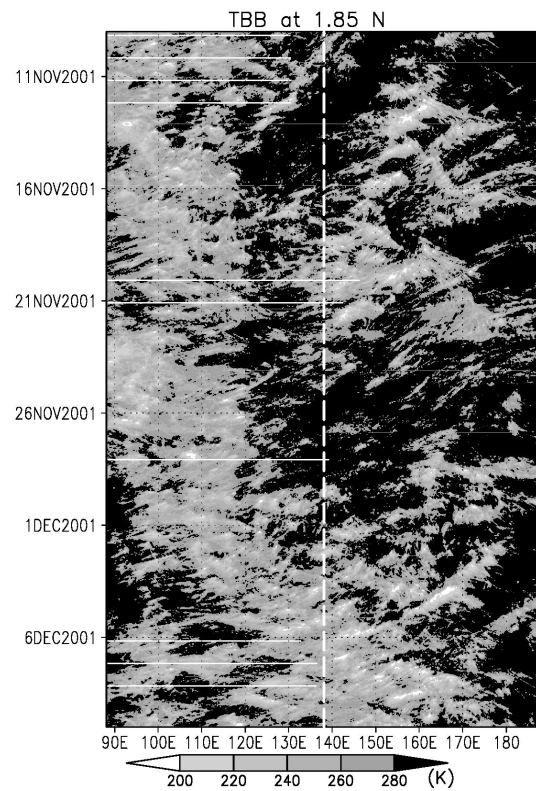


Figure 1: Time-longitude cross-section of infrared equivalent blackbody temperature. Data are from the Geostationary Meteorological Satellite of the Japan Meteorological Agency. Dashed line indicates the longitude of R/V *Mirai*.

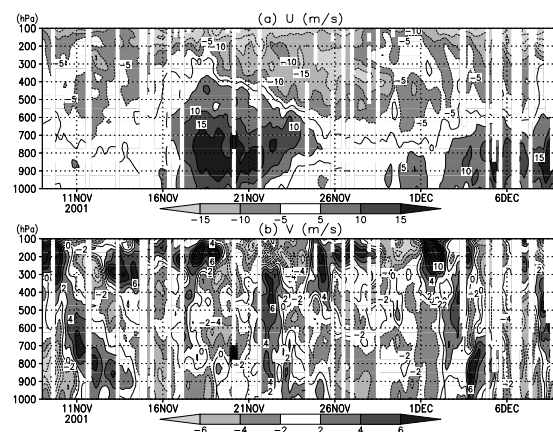


Figure 2: Time-height cross-sections of (a) zonal and (b) meridional wind components derived from

radiosonde. Observations were conducted every 3 hours from 0000 UTC, November 9 until 0000 UTC, December 9. Solid and dashed contours indicate positive and negative values, respectively. Periods of no data are left blank.

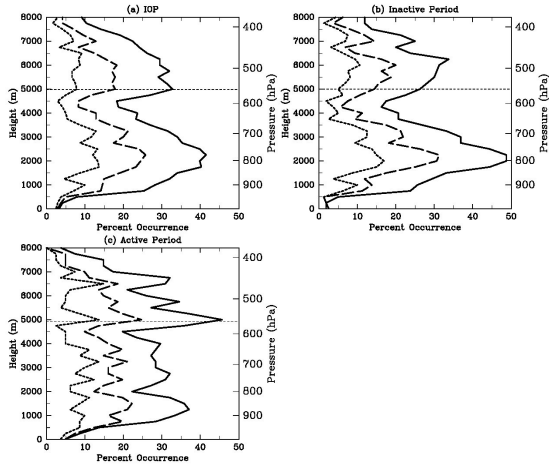


Figure 3: Cumulative frequency of stability (dT/dz) for values greater than -5 (solid lines), -4.5 (dashed lines), and -4 K km^{-1} (dotted lines) during the IOP (a), inactive period (b), and active period (c). Thin dotted line in each panel indicates the 0°C level.

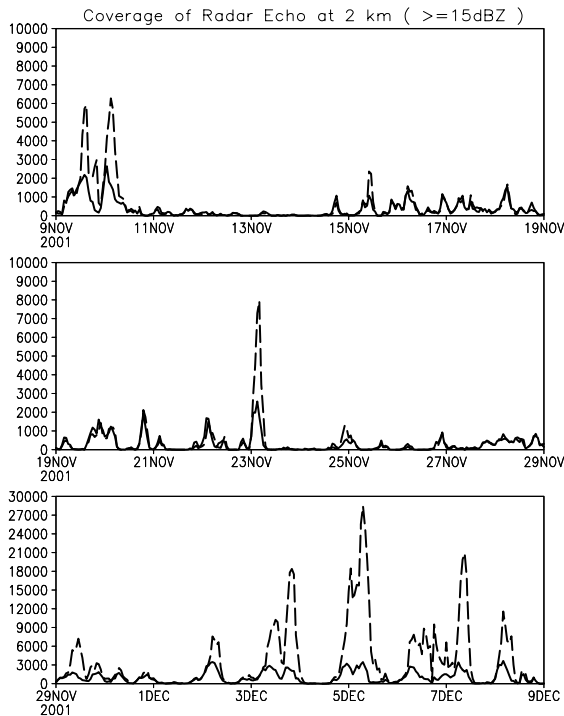


Figure 4: Evolution of the coverage of C-band radar

echo for reflectivity factors $>15 \text{ dBZ}$ at 2 km height over a $200 \text{ km} \times 200 \text{ km}$ area during the IOP (unit: km^2).

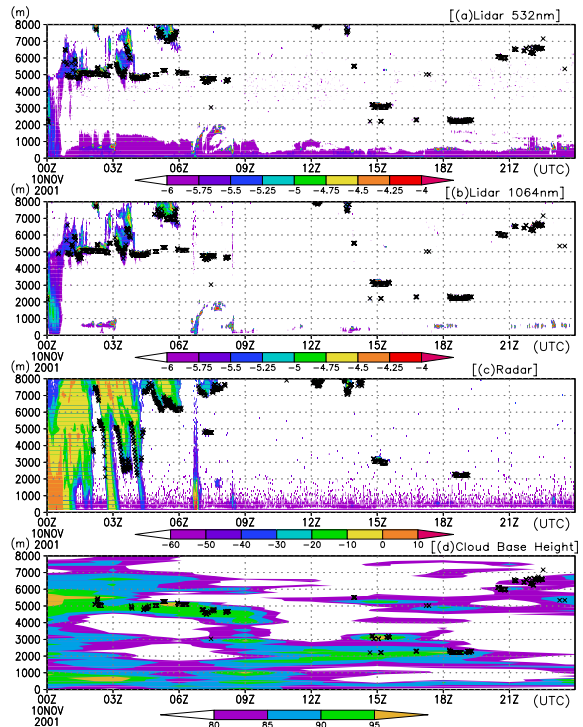


Figure 5: Time-height cross-section of 532 nm lidar backscattering coefficient (a), 1064 nm-lidar backscattering coefficient (b), radar reflectivity factor (c), and ultimate cloud base (Z_b) distributions (d). Crosses in the upper three figures indicate the levels where the backscattering coefficient and reflectivity first exceeded certain thresholds during the vertical scan from the height of 2 km (see text for details). In the lowest panel, the area with high relative humidity ($>80 \%$) is shaded by colorscale.

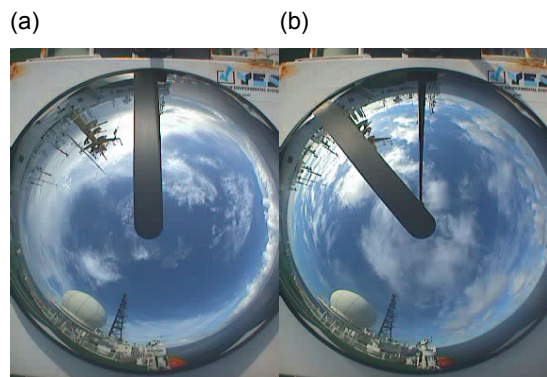


Figure 6: TSI images taken at (a) 0611 UTC, and (b)

2211 UTC on 10 November 2001

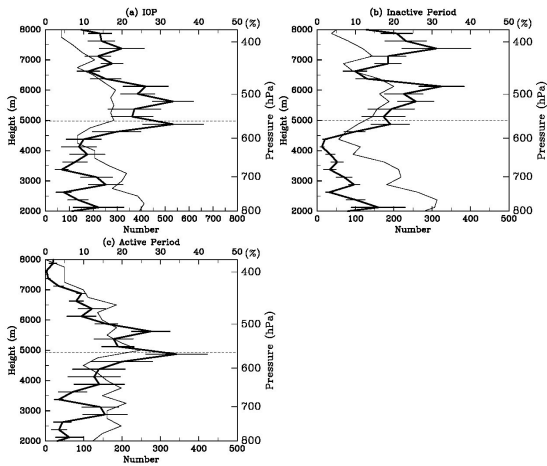


Figure 7: Frequency distribution of the base heights of thin cloud layers (thick solid lines) during the IOP (a), inactive period (b), and active period (c). Error bars represent the ranges within one standard deviation calculated from 30 samples. Cumulative frequency of stability (dT/dZ) for values greater than -4.5 K km^{-1} (see Fig. 3) and the 0°C level are overplotted in each panel with thin solid and dotted lines, respectively.

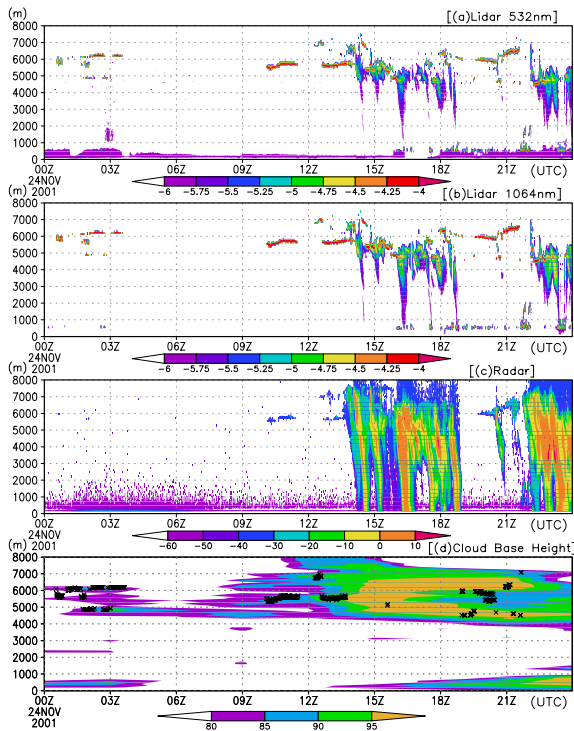


Figure 8: Time-height cross-section of 532 nm lidar backscattering coefficient (a), 1064 nm lidar

backscattering coefficient (b), radar reflectivity factor (c), and ultimate cloud base (Z_b) distributions (d) on 24 November 2001. In the lowest panel (d), the area with high relative humidity ($>80\%$) is shaded by grayscale.

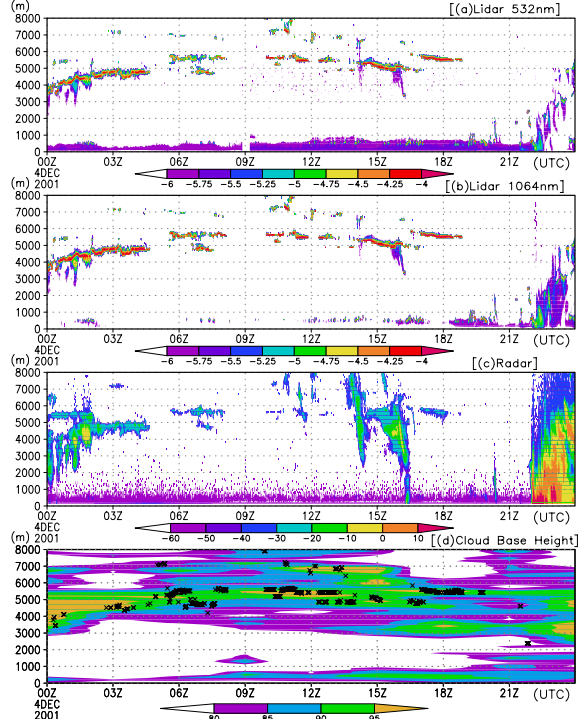


Figure 9: The same as Fig. 8, except on 4 December 2001.

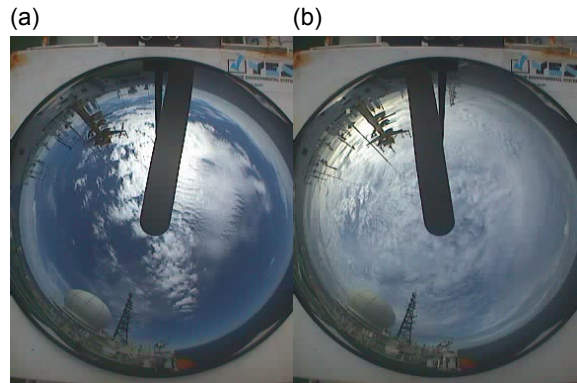


Figure 10: TSI images taken at (a) 0041 UTC on 24 November, and (b) 0711 UTC on 4 December 2001

Table 1: Occurrence frequency (%) of the thickness of the cloud whose base (Z_b) is located between at 4.5 - 6.5 km height. Clouds are identified as objects

with a lidar backscattering coefficient exceeding -5.25 ($= \log_{10} \beta$, where β ($\text{m}^{-1} \text{sr}^{-1}$)).

	IOP	Inactive	Active	
	0-82.5	31.1	33.2	28.4
	82.5-165	34.4	34.8	33.9
	165-247.5	20.4	21.7	18.7
Thickness	247.5-330	9.4	6.8	12.7
(m)	330-412.5	3.5	2	5.4
	412.5-495	0.9	0.8	1
	495-577.5	0.3	0.4	0
	577.5-660	0.1	0.1	0

Table 2: Occurrence frequency (%) of the thickness of the cloud whose base is located between at 4.5 - 6.5 km height. Clouds are identified as areas with the relative humidity exceeding 95 % or 85 %.

	IOP		Inactive		Active	
	>9	>85	>95	>85	>95	>85
	5%	%	%	%	%	%
0 -						
100	26	30	24	38	28	17
100-						
200	22	18	12	19	28	17
200-						
300	4	10	4	8	4	15
300-						
400	12	6	8	3	14	10
400-						
500	3	7	4	5	2	10
500-						
600	4	4	8	5	2	2
600-						
700	5	4	12	6	2	2
700-						
800	7	2	12	1	4	2.1
800-						
800-	17	19	16	16	18	25